# Experimental Analysis of the Aerodynamics of Long-Shrouded Contrarotating Rotor in Hover




Chao Huo*
*Associate Researcher*

Roger Barènes
*Senior Researcher*

Jérémie Gressier
*Associate Professor*

*Institut Supérieur de l'Aéronautique et de l'Espace, PRES Toulouse, France*



**This paper aims to quantify the benefits of a shrouded coaxial rotor configuration through experimental comparisons with free (not shrouded) rotors in hover. The experiment shows that both the figure of merit of contrarotating rotors and the system power loading are improved by the shroud inclusion. Improvements are induced by a suction effect at the inlet, which can be optimized by a regulation effect of the mass flow. Compared to free rotors, the strong suction peak formed on the shroud leading edge by a 65% increase in mass flow, allowing the shroud to contribute up to 56% of the total thrust. More uniform pressure distribution in the downstream rotor and less contraction of the slipstream decrease losses and increase the rotor efficiency. The shrouded system efficiency is further improved if the upstream rotor rotates slower than the rear one, for a given total shaft power, because a stronger pressure depression occurs upstream of the rotors to generate more mass flow. On the other hand, the system behavior is insensitive to the interrotor distance.**


## Nomenclature

| | |
|---|---|
| $A_r$ | rotor disk area, $m^2$ |
| $C_{P_s}$, $C_{P_t}$ | static and total pressure coefficients |
| $D_{abs}$ | absolute distance from the shroud inlet to the first rotor, mm |
| $F$ | thrust, N |
| $\dot{m}$ | mass flow rate, kg/s |
| $N$ | rotational speed of the rotor, rpm |
| $Q$ | torque, N·cm |
| $R_{max}$ | maximum radius of the shrouded system at the local longitudinal station, mm $R_r$ rotor radius, mm |
| $V_{ind}$ | local induced velocity, m/s |
| $\overline{V_{ind}}$ | mean induced velocity at the rotor disk, m/s |
| $W_{mech}$ | total mechanical power, W |
| $\beta_{root}$ | blade pitch angle at the root, ° |
| $\beta_{tip}$ | blade pitch angle at the tip, ° |

### Subscripts

| | |
|---|---|
| $j$ | tested circumferential rings at longitudinal stations |
| $t$, sh, $r_i$ | components of the system, $t$ for the whole shrouded system, sh for the shroud, $r_i$ for the rotor ($i = 1$ for front rotor, 2 for rear rotor) |


*Corresponding author; e-mail: huochao1023@hotmail.com.


Manuscript received October 2013; accepted April 2015.


## Introduction

One of the most important requirements for micro unmanned air vehicles (MAVs) operating in indoor or urban canyon conditions is that MAVs should be able to loiter for a long period in stationary or quasi-stationary flight: This means a highly efficient hover capability. It makes rotary-wing vehicles face unique challenges. Owing to the small size and low speed, MAVs usually operate at low Reynolds numbers, a domain where the viscous effects take a dominant role in determining the performance. The research on the aerodynamics of conventional small-scale single or coaxial rotor systems revealed that vehicles suffer from high power consumption and low rotor efficiency (or figure of merit, FoM) because of the airfoil performance deterioration at low Reynolds numbers as discussed in Refs. 1–5. Owing to the flow separation, transition, and reattachment, Refs. 6 and 7 revealed that the maximum efficiency of microrotors can drop to 0.2, whereas full-scale helicopter can reach to 0.8 under a similar disk loading (Ref. 8). One possible solution is enclosing the rotors in a shroud, provided that the shrouded rotor system compensates for the additional shroud weight.

Based on this concept, a shrouded or ducted contrarotating rotor system was proposed with several design and operational benefits. The employment of the shroud promises to enhance the aerodynamic capabilities. It has been utilized in Fenestron tail rotors (Refs. 4 and 5) and vertical take-off and landing (VTOL) unmanned aerial vehicles (UAVs) (Refs. 9–11). Furthermore, shrouds offer an attractive solution for providing protection to the rotating blades and a convenient structure for mounting additional hardware. In regard to contrarotating rotors, although they generally produce greater loss than two individual rotors at same disk loading, the elimination of a separate antitorque system

provides a benefit of reducing the system weight. The combination of the shroud and coaxial contrarotating rotors takes advantages of the merits of each isolated system.

Since the 1960s, many studies have been performed on large-scale shrouded rotors (Refs. 12–14). However, these works are still limited in applicability to small-scale UAVs since they do not address the physics that govern small-scaled shrouded rotors operating in low Reynolds number flow regime. Recently, there has been extensive research into systematic design, testing, and computational investigations of small-scale shrouded single rotors (SSRs) in hover (Refs. 9–11, 15, 16). In particular, Pereira and Chopra (Ref. 17) experimentally performed an extensive shroud parametric study. They revealed the different effects of each shroud design parameter on the performance. Hrishikeshavan et al. (Ref. 18) applied this knowledge to design a shrouded single-rotor MAV. They indicated that, compared to a free rotor, a shrouded rotor has a 40% improvement in power loading. Their work provides a good guidance and example to design a shroud. However, their experimental identification is basically focused on a SSR, which does not account for the complex swirl flow between coaxial rotors. Lakshminarayan and Baeder (Ref. 19) determined the flow physics explaining the shroud's contribution to the total thrust through a computational investigation. While their study assumed a fully turbulent flow in all regions, in fact, it is very difficult to precisely determine the location of the flow transition through the shroud using numerical methods. Specifically focusing on the shrouded contrarotating rotor configuration, Lee et al. (Ref. 20) revealed that the aerodynamic forces on the duct itself recovered the net system thrust. They examined the system performance under different flight states. Their experimental setup could not separately evaluate two rotors and a shroud. This setup limited the exploration on interactions between different components. Based on the limitations of the above research, the influence of the shroud on the flow field needs to be further explored to better understand the shroud's role on such a system and better guide its design. Moreover, since the aerodynamic interactions of two rotors and the shroud play a critical role in improving the system, hover testing needs to consider additional rotor attributes such as the speed of the individual rotors and rotor locations. These design considerations make it essential to measure the contribution of each component separately.

Based on one optimally designed shroud in Refs. 21 and 22 and a set design for a pair of rotors, this paper aims to quantify the benefits of the shroud and to understand the corresponding physics. To support the global performance analysis, two characteristic diagrams have been proposed to adapt classical parameters to shrouded coaxial rotor systems. To ensure an accurate and valid explanation of the advantages of a shrouded system, the flow characteristics of an unshrouded system have been analyzed and the two are compared. This process included the examination of pressure measurements at several longitudinal positions and on the shroud wall.

Furthermore, regardless of the shroud profile, by switching speeds and changing rotor locations inside the shroud, the local aerodynamic effects on the flow generation have been analyzed to identify further improvements.

## Experimental Setup and Design

### Experimental setup

An experimental test bed was designed and fabricated with stability, precision, and flexibility considerations. It was used to understand the flow physics and the interaction between different components of the shrouded contrarotating rotor. Besides the individual performance parameters such as thrust and torque, the test bed can measure the evolution of aerodynamic variables that characterize the flow passing through the shroud, such as total and static pressure. In this paper, the global performance parameters are obtained directly from experiments. For the aerodynamic analysis, the measured pressure distribution along the shroud wall as well as the total pressure and static pressure at different longitudinal locations are used to calculate velocities and mass flow.

*Test bed.* Figure 1 presents a detailed overview of the test bed layout. To minimize external influences on the rotor system performance, a distance

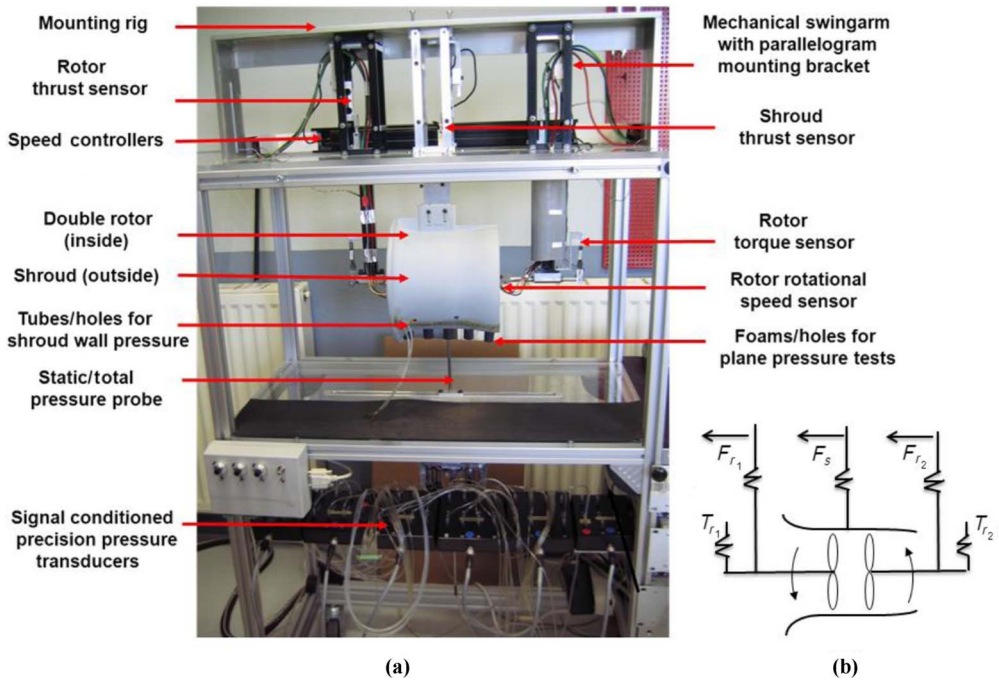


**Fig. 1. Test bed configuration (a) and simplified working schematic (b).**

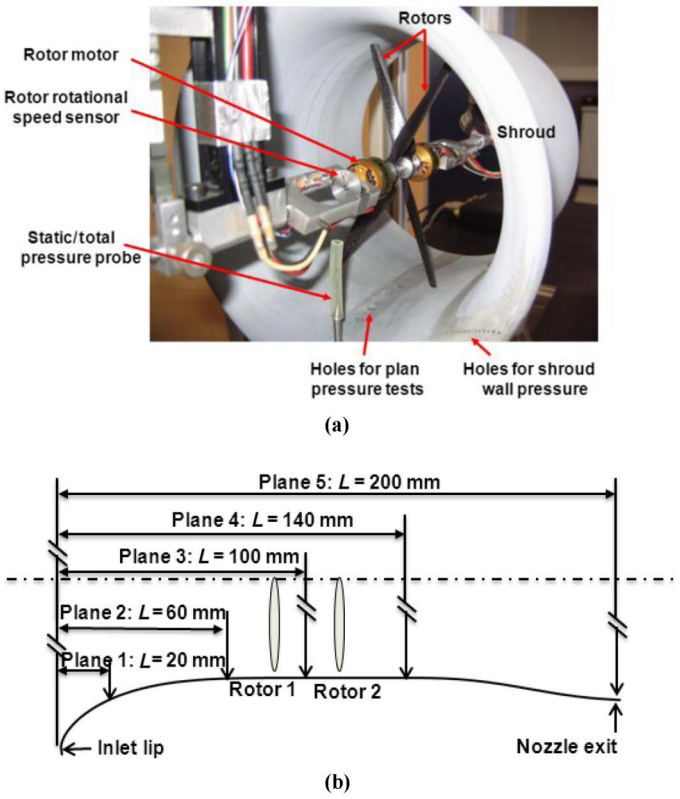


**Fig. 2. Configuration of shrouded contrarotating propulsion system (a), positions of tested longitudinal planes (b), and shroud profile (c).**

at least 10 times the size of the rotor diameter downstream of the test bed should have no obstructions. The shroud and two rotors are supported by three independent mechanical swingarms. Hence, this test bench is able to test four different systems: free single rotor (FSR), free double rotor (FDR), SSR, and shrouded double rotor (SDR). The mechanical swingarms are connected to parallelogram structures mounted on the top of the rig, allowing the location of the two rotors to change inside the shroud.

Various sensors are used to measure the overall performance. Thrust sensors on each rotor and on the shroud are installed within three parallelogram structures to allow for separate but simultaneous measurement of the thrust produced by each rotor and the shroud. Figure 2(a) shows the aluminum mounting brackets, which connect the brushless motors to the mechanical swingarm. The rotational speed of each rotor is measured with a small circular disk installed in the axle of each motor. Torque sensors are located at the end of each axle. This setup gives the flexibility to separately evaluate the different components on their overall performance by measuring thrust, torque, and power.

**Table 1. Rotor parameters**

| Parameter | Front Rotor Value | Rear Rotor Value |
|---|---|---|
| Root radius (mm) | 9.6 | 9.6 |
| Tip radius (mm) | 88.9 | 88.9 |
| Root chord (mm) | 13.2 | 13.2 |
| Tip chord (mm) | 6.4 | 6.4 |
| $\beta_{root}$ (°) | 42.2 | 41.3 |
| $\beta_{tip}$ (°) | 18.6 | 18.1 |

To understand how the shroud contributes to the thrust, 36 test positions were distributed on the shroud wall for the static measurements of the wall pressure, as shown in Fig. 2(a). At the shroud inlet, pressure measurements are more highly concentrated, due to the importance of pressure gradients at this location.

To investigate flow characteristics, the static/total pressure values were obtained using total and static pressure probes set at several selected longitudinal stations (see Fig. 2(b)). Each probe is able to measure the pressure in axial and tangential directions for an adjustable radial position. Measurements are difficult to converge when the probe is close to the blade. Therefore considering the probe accuracy and safety, the distance from the test position to the rotor is kept at least 20 mm.

*Model: Shrouded contrarotating rotor.* The model in Fig. 1 consists of a 180-mm-main-inner-diameter shroud and two contrarotating two-bladed rotors installed in the same axis as the shroud.

The optimal shroud was designed according to the past experiments in Ref. 21 and the two-dimensional axisymmetric simulations in Ref. 22. The shroud consists of three parts: inlet, middle section, and nozzle. The lengths of three different parts are $0.9R_r$, $0.45R_r$, and $0.9R_r$, respectively. Its specific geometric parameters are shown in Fig. 2(c).

A pair of the contrarotating rotors was specifically designed for shrouded systems using the code XROTOR, which was developed by Drela and Youngren (Ref. 23) with nonzero circulation at the blade tip. It is based on the classical vortex/blade-element methods of Betz (Ref. 24) and Glauert (Ref. 25) and a general three-dimensional vortex-lattice or panel method. All of the blade parameters are summarized in Table 1.

## Experimental design

*Design variables.* The experiments were designed for several objectives. First, to explore the influence of the shroud, the shrouded contrarotating rotor was compared to FDR. Both the characteristics of the shrouded system and the benefits from the shroud were evaluated in terms of global performance. Furthermore, to investigate the aerodynamic effects from the shroud, the pressure fields of shrouded and open systems were compared; the wall pressure distributions at several rotational speeds with different speed intensities were tested. Both measurements aimed to understand and sustain the improvement caused by the shroud. To further enhance the ability of a given shroud to aspirate the air, various rotor speeds and different rotor locations were tested to examine the shroud local aerodynamic effects through both wall pressure and field pressure measurements. Rotor locations include interrotor distance (IRD) and absolute distance from the shroud inlet to the first rotor ($D_{abs}$). Table 2 presents the variables and their regimes for different measurements.

As Table 2 shows, both shrouded and free systems were tested at rotational speeds from 4000 to 9000 rpm; 4000 rpm was the lowest

**Table 2. Design variables and regimes**

| Test | Shroud Benefit (SDR and FDR) | Aerodynamic Study for Different Controls of Rotors | | | |
|---|---|---|---|---|---|
| | | Symmetric Speeds | Switching Speed | Rotor Locations | |
| Design variables | $N_1 = N_2$(rpm) | $N_1 = N_2$ (rpm) | $N_1 \neq N_2$ (rpm) | $D_{abs}/R_r$ | IRD/$R_r$ |
| Range | [4000: 9000] | (4000,4000)<br>(6000,6000)<br>(8000,8000) | (6000, 9000)<br>(9000,6000) | 0.9 | 0.2,<br>0.4 |

speed at which the two-rotor system was tested, because the performance is more sensitive to the interactions between two rotors with reduced speeds and becomes very unsteady. 9000 rpm is sufficient to produce a total thrust 5 N required to sustain the whole vehicle's weight in hover.

Within the compared speed range mentioned above, a rotational speed of 6000 rpm was tested to identify the shroud influence on the pressure field since the measurements become more stable at this speed. Meanwhile, three pairs of rotational speeds, 4000, 6000, and 8000 rpm, were chosen to show the shroud local effects under different air mass flow rates. To enhance the ability to understand flow generation through the rotor configurations, first, one speed pair, 6000 and 9000 rpm, was chosen, because the slower rotor can still produce a thrust even under the influence of another rotor which rotates faster. These rotational velocities correspond to the blade tip speeds of 56 and 84 m/s. Both speeds result in local Mach numbers less than 0.24. Additionally, the interrotor distance is always expected to be as short as possible due to the constraints of the vehicle's size and weight. Two IRDs of 0.2 and 0.4 times the rotor radius were therefore selected. The distance between the two rotors is limited to $0.2R_r$ to avoid interference between the rotors. These two IRDs together with the absolute distance $0.9R_r$ ensure that two rotors are located in the shroud cylindrical section, which has the minimum shroud diameter (see Fig. 2(c)). By constraining the rotor location to the cylindrical section of the shroud, the shroud-to-tip gap is minimized to reduce the tip vortex losses (Fig. 7 in Ref. 9) and to allow a sufficiently large zone aft of the rotors for the flow expansion.

*Performance indicators: Power loading and figure of merit.* Two variables were used to evaluate the performance of the system:

1) *The power loading* (PL). It defines the dynamic performance of the whole system and indicates the capability of a system to convert the available mechanical power into the thrust for a given disk area. It is expressed as

$$\mathrm{PL} = \frac{F_t}{W_{\mathrm{mech}}} = \frac{F_{\mathrm{sh}} + \sum_i F_{r_i}}{\sum_i \left| Q_{r_i} \omega_{r_i} \right|} \tag{1}$$

2) *The figure of merit* (FoM). It is a measure of the efficiency of the two-rotor system. It quantifies the ability of rotors to convert available shaft power into the induced power working on the surrounding fluid (i.e., kinetic energy and static enthalpy induced on the fluid):

$$\mathrm{FoM} = \frac{\dot{m} \cdot \left[ \left( \frac{1}{2} V_e^2 - \frac{1}{2} V_\infty^2 \right) + \left( \frac{P_e - P_{\mathrm{atm}}}{\rho} \right) \right]}{W_{\mathrm{mech}}} \tag{2}$$

Since the variables such as the total thrust $F_t$, the shroud thrust $F_{\mathrm{sh}}$, the rotor thrust $F_r$, the torque $Q_r$, and the angular speed of each rotor are obtained through measurements, the performance PL is calculated directly. The FoM (Eq. (2)) is further simplified and adapted for experiments. For the adapted nozzle, the exit pressure $P_e$ is equal to the ambient one $P_{\mathrm{atm}}$. Based on the Bernoulli theorem, Eq. (2) is written as

$$\mathrm{FoM} = \frac{\dot{m} \cdot \left[ \left( \frac{1}{2} V_e^2 - \frac{1}{2} V_\infty^2 \right) \right]}{W_{\mathrm{mech}}} = \frac{\dot{m} \cdot \left[ \frac{(P_{\mathrm{up}} - P_{\mathrm{down}})}{\rho} \right]}{W_{\mathrm{mech}}} \tag{3}$$

The thrust of the two rotors is due to the pressure differential, $\Delta P = P_{\mathrm{up}} - P_{\mathrm{down}}$, across the rotor system. It is calculated as $F_r = \Delta P A_r$, where $A_r$ is the rotor disk area. Combined with the mass flow rate expression, $\dot{m} = \rho A_r V_{\mathrm{ind}}$, where $V_{\mathrm{ind}}$ is induced flow velocity from momentum theory. Equation (3) can be simplified in two ways:

$$\mathrm{FoM} = \frac{\dot{m} F_r}{\rho A_r W_{\mathrm{mech}}} = \frac{F_r V_{\mathrm{ind}}}{W_{\mathrm{mech}}} \tag{4}$$

*Main variables and nondimensional parameters.* The local induced velocity, $V_{\mathrm{ind}}$, was calculated as a circumferential value at longitudinal stations through the measurements of the static pressure, $P_s$, and the total pressure, $P_t$ (see Eq. (5)). The mass flow is obtained by the integration of the air passing through each circumferential ring, $j$, in Eq. (6):

$$V_{\mathrm{ind}} = \sqrt{\frac{2(P_t - P_s)}{\rho}} \tag{5}$$

$$\dot{m} = \sum_{j=1}^{n} \pi \left( R_{j+1}^2 - R_j^2 \right) \rho V_{i_j} \tag{6}$$

After simplification, two performance indicators introduced above can be derived from the measurements of the basic quantities such as thrust, torque, pressure, and so on. These quantities were corrected to a standard atmospheric condition, $T_{\mathrm{stan}} = 288.15$ K and $P_{\mathrm{stan}} = 101325$ Pa, thereby eliminating external perturbations and possible weather variations.

To facilitate the analysis, the pressure coefficient, $C_p$, was employed to analyze the static or total pressure distributions on the shroud and at longitudinal stations for different configurations. It is defined as in Eq. (7):

$$C_p = \frac{(P - P_{\mathrm{atm}})}{\frac{1}{2} \cdot \rho \cdot \overline{V_{\mathrm{ind}}}^2} \tag{7}$$

where $P$ is static pressure $P_s$ or total pressure $P_t$. $\overline{V_{\mathrm{ind}}}$ is the mean induced velocity on the rotor disk, as defined in Eq. (8):

$$\overline{V_{\mathrm{ind}}} = \frac{\dot{m}}{\rho \cdot A_r} \tag{8}$$

However, the definitions of two nondimensional parameters, thrust coefficient $C_T = F/\rho A_r N^2 R_r^2$ and power coefficient $C_w = W/\rho A_r N^3 R_r^3$, cannot be easily adapted as discussed in Ref. 26, because our system involves the interaction between two rotors, which might be operating at different rotational speeds. Since the main objective of this work is not to compare with other rotors, but to explore the shroud's role in system

**Table 3. Accuracy of measurements**

| Parameter | Mechanical Accuracy | Calibration/Reading Error | Total |
|---|---|---|---|
| Thrust (N) | ±0.05 | ±(0.6%) | $\pm(0.05 + 0.6\%F)$ |
| Torque (N·cm) | ±0.02 | ±(0.7%) | $\pm(0.02 + 0.7\%Q)$ |
| Rotational velocity (rpm) | ±50 | ±14 | ±(50 + 14) |
| Wall static pressure (Pa) | ±1 | ±5 | ±(1 + 5) |
| Plane static pressure (Pa) | ±1 | ±3 | ±(1 + 3) |
| Plane total pressure (Pa) | ±1 | ±3 | ±(1 + 3) |

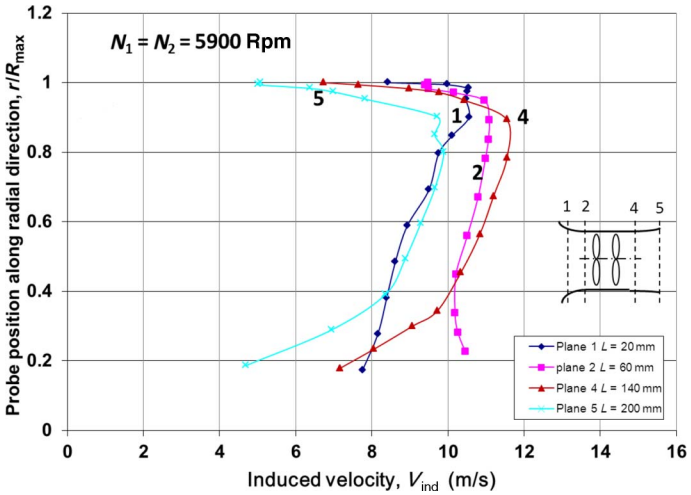


**Fig. 3. Induced velocity at different longitudinal stations for the SDR system.**

behavior and its ability to define the stream tube, the analysis on the overall system performance is hence conducted using dimensional values.

### Uncertainty and evaluation

The precision and resolution of measurements were evaluated by the characteristics of sensors and the acquisition system provided by manufactures. The mechanical accuracy is defined as the smallest load, rotational speed, or pressure, which can be measured by the respective sensor. Standard deviation of the sampled data was used to determine the uncertainty of the measurement, according to the method of Kline and McClintock (Ref. 27). Table 3 shows the uncertainty of every tested variable.

According to the uncertainty above, the principle performance (PL) can be precisely evaluated. Another performance indicator (FoM) needs to be further validated since the induced velocity cannot be directly obtained by measurements. Figure 3 shows the radial distribution of induced velocity at different longitudinal stations for a SDR system. Owing to the larger cross-sectional area of the shroud, the inlet plane 1 and the outlet plane 5 have a lower induced velocity than other two planes, which are close to the beginning and the end of the shroud cylindrical section, respectively. Downstream of the two rotors, the induced velocity near the shroud wall and the hub tends to greatly decrease due to the boundary layer, leakage flow, and swirl loss.

Based on the data in Fig. 3, the global mass flow rate and averaged $V_{ind}$ are compared at different planes, as shown in Table 4. The mean induced velocities at planes 2 and 4 are very similar to each other and higher than the velocities at the other two planes. Since the flow is incompressible, the differences of the mean induced velocity at different longitudinal

**Table 4. Mass flow and mean $V_{ind}$ at different planes for the SDR system**

| SDR | Area ($m^2$) | Mass Flow (kg/s) | Mean $V_{ind}$ (m/s) |
|---|---|---|---|
| Plane 1 | 0.0291 | 0.320 | 9.0 |
| Plane 2 | 0.0255 | 0.316 | 10.1 |
| Plane 4 | 0.0260 | 0.321 | 10.1 |
| Plane 5 | 0.0302 | 0.308 | 8.3 |

stations can be partially explained by the different areas and also by the use of three-hole probes for measurement—a measurement method that is more accurate when radial velocity components are negligible. The mass flow is found to be conserved through all of the planes. The greatest change in mass flow occurs at the nozzle exit, where approximately 4% (0.013 kg/s) less mass flow was measured than at plane 4. However, at the nozzle exit such a difference is acceptable since a part of flow measurement occurs in the mixing boundary between the ejected flow and the ambient flow. The flow field measurements above indicate that the two probes have good accuracy, and they will be used for the aerodynamic tests.

## Results and Discussion

The global characteristics of the shrouded system are first discussed in terms of the effect of the shroud. The potential physics are analyzed by comparisons of the FDR system overall performance and aerodynamics. To further improve the rotor configuration, different situations are studied: the rotational speeds of three intensities, switching rotational speeds, and two pairs of rotor locations situated in shroud cylindrical part.

### Characteristics and shroud benefits of SDR

The experimental work in Ref. 21 indicates that SDR with the rotor locations $D_{abs} = 0.9R_r$ or 80 mm and IRD $= 0.2R_r$ or 20 mm (SDR80-20) performs best, so all experiments of SDR to explore the shroud benefits were done with rotors at these locations.

*Overall performance of SDR.* To more comprehensively quantify the global performance where the two rotors are operated at two different speeds, a new double $N$ diagram (Fig. 4) was developed to replace the traditional propeller diagrams.

For the whole system SDR80-20, PL is improved with lower rotational speed, due to the effect of lower disk loading. The region highlighted in blue in Fig. 4 indicates an optimal performance region in which the system produces maximum thrust but consumes minimum power. Within this region, the isototal thrust line is tangential to the iso-PL line. It can be observed that this optimal region has the second rotational speed $N_2$ greater than the first one $N_1$. This condition is in conflict with the requirement of zero total torque. The speed region with optimum PL is not located where the torque is balanced. This unbalance behavior comes

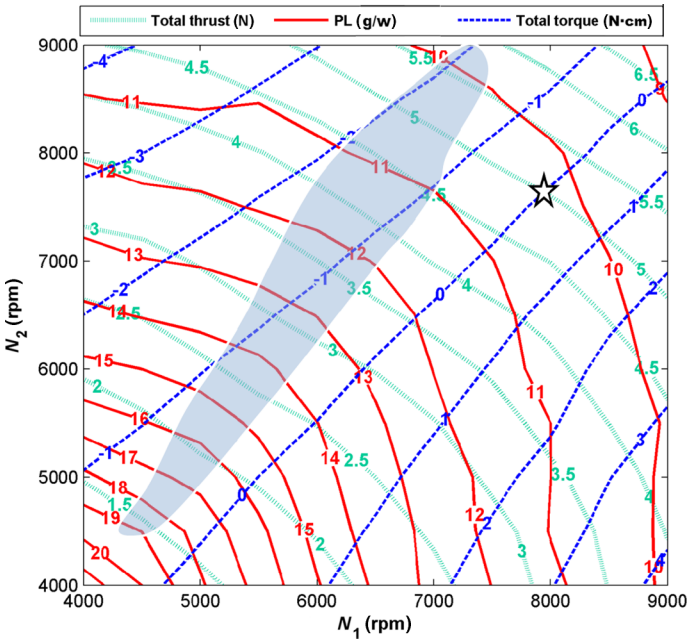


**Fig. 4. Iso performances versus $N_1$ and $N_2$, SDR80-20.**

from the interaction between the two rotors. It also reveals that there is room for improvement in the blade design, particularly in the pitch angle.

*Shroud benefits on global performance.* To determine the benefits from the shroud, the same double rotor, which is open instead of shrouded, was compared to the SDR system. The inter distance $0.4R_r$ (40 mm), which performs best among the distances from 20 to 90 mm (Ref. 28), was applied for the FDR system.

The effect of the shroud presence on the mass flow rate (Fig. 5(a)) indicates that an increased mass flow is generated by the shrouded system compared to the free one. This improvement consistently remains around 65%. Since the shroud inlet was designed to adapt the flow, it is considered to be consistent with the stream tube boundaries of FDR. The strong ability to aspirate the mass flow is greatly affected by the nozzle exit area design. Compared to the theoretical value of 0.5 for FDR, an exit-to-rotor disk area ratio of 1.2 adequately expands the flow downstream of the rotor, decreases the final wake velocity, and ultimately increases the mass flow inside the shroud.

The increased mass flow over the shroud directly reflects an improvement of system thrust performance, as shown in Fig. 5(b). Compared to free rotor systems, the total thrust of shrouded rotors is augmented from 63% up to 80% with increased power. The shroud plays an important or full role in this augmentation since it can contribute more than half of the total thrust. With increased power input, the ratio of the shroud thrust over the total thrust shows a negative second derivative augmentation and tends to be constant under increased power input. The maximum benefit might happen between 20 and 40 W input power.

Figures 5(c) and 5(d) indicate an improved PL performance and FoM of the shrouded system for a given total shaft power, compared to the free system. The improvement comes from the substantial increase of the mass flow and the total thrust from SDR systems. Corresponding to the thrust performance in Fig. 5(b), the greatest PL improvement occurs at the highest power input. The shrouded system appears to be much more efficient than the free system. It is able to induce more of the input mechanical shaft power into the flow in terms of the kinetic energy. Nevertheless, the comparison was made on the basis of the rotors originally designed for the shrouded system, which are prone to generate more tip vortices than rotors originally designed for free stream. Compared to the maximum efficiency of 0.65 for free rotor systems from the current studies (Ref. 29), this shrouded rotor system having an efficiency above 0.7 still indicates the benefit from the shroud.

Figure 5(e) provides a visual representation of each rotor thrust. The shroud significantly changes the upstream rotor thrust, while the rear rotor thrust experiences minimal change. The aerothermodynamic upstream conditions are greatly modified by the shroud presence, and the enlarged outlet section allows both rotors to aspirate more mass flow than a free stream system, where the downstream natural contraction of the flow is theoretically half of the disk rotor area. Even though the upstream rotor thrust is greatly decreased, it can be completely compensated by the shroud thrust created by the increased mass flow, as shown in Fig. 5(b).

The improvements of shrouded systems noted in PL and FoM are generally due to a greater mass flow and lower pressure behind the second rotor compared to the free system. This large flow aspiration of the shrouded contrarotating system was further explored by the measurements of its flow field pressure.

## Aerodynamic analysis

*Shroud effect: Pressure field measurements.* For SDR80-20, it is difficult to perform measurements at a plane between the rotors due to the close rotor-to-rotor spacing. Therefore, measurement planes upstream and downstream of the two rotors and at the nozzle exit were chosen. Figure 6 presents the distribution of static and total pressure coefficients at each plane, plus the FDR downstream plane.

Figure 6(a), the shrouded rotor system case, the total pressure coefficient distributed along the radial direction is not uniform downstream of the two rotors. The flow gains the energy induced by the two rotors; thereby the pressure significantly increases after the two rotors. Overall, the total pressure coefficient at the shroud exit is slightly lower than at plane 4 due to friction losses and flow swirl. The two main sources of losses through the shroud are observed: First, a large drop of total pressure near the shroud wall occurs due to both the shroud boundary layer and blade tip vortices downstream of the rotors. Second, the total pressure decreases close to the hub because of the swirl in the flow generated around the blade root.

Compared to the SDR at plane 4, the FDR has a much smaller effective stream tube area due to the more contracted flow, even though a greater total pressure level in the main region of the stream tube is obtained. The total pressure at $r/R_{\max} > 0.85$ already approaches the ambient pressure. Around this radial location, the FDR is strongly influenced by a mixing flow boundary. Evidently the pressure loss caused by the blade tip vortex is far greater than SDR. These phenomena further imply that the presence of the shroud effectively produces a more uniform pressure distribution, substantially reduces the slipstream contraction, and minimizes the blade tip loss. It has the same effect as the bypass ratio in a turbofan, decreasing the maximum velocity but enlarging the air mass flow, and improving the system propulsive efficiency.

Figure 6(b) shows that the static pressure distribution at each plane is almost constant. A relatively good radial equilibrium is reached due to the absence of any swirl in the nozzle portion of the shroud. At plane 2, located upstream of the rotors, the total pressure generally remains at zero and the flow is accelerated by the curved shroud profile, the static pressure at this plane reaches a minimum value compared to other two planes which benefit from the induced power. Compared to unshrouded systems, in which the static pressure is always equal to the ambient pressure, the shroud allows a lower static pressure to be formed especially

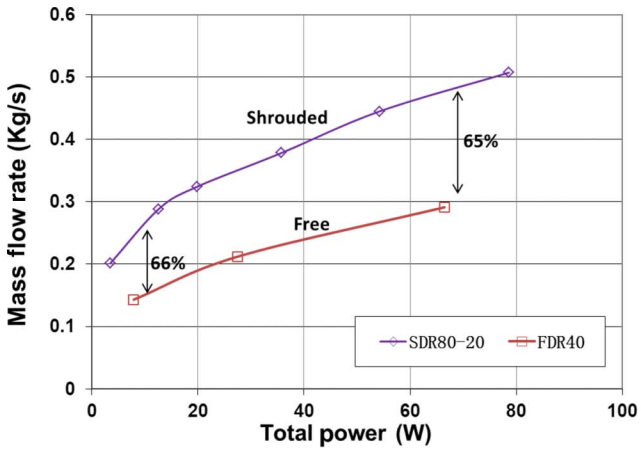


(a)

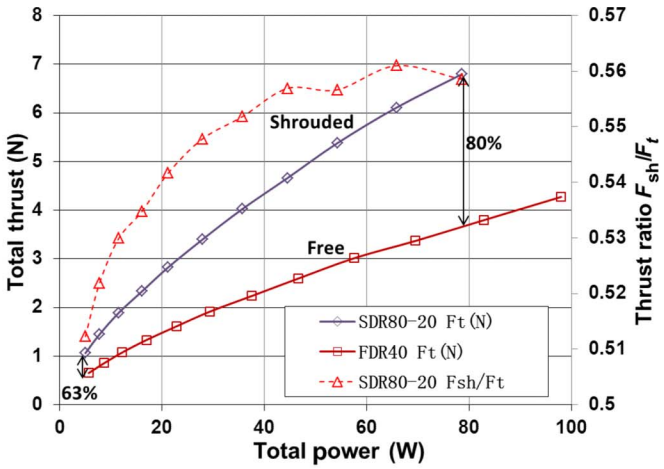


(b)

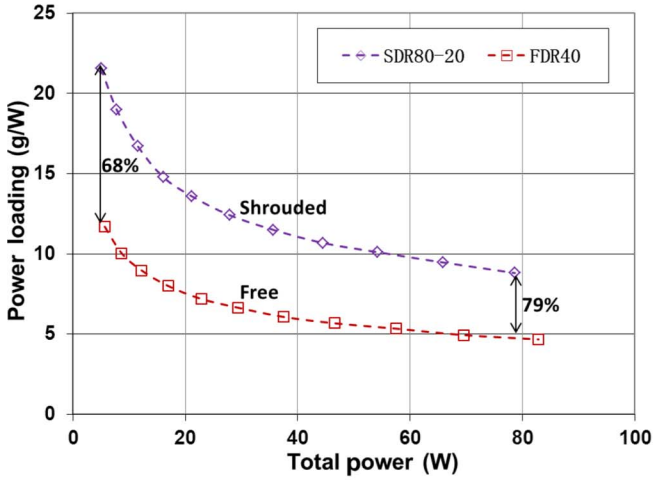


(c)

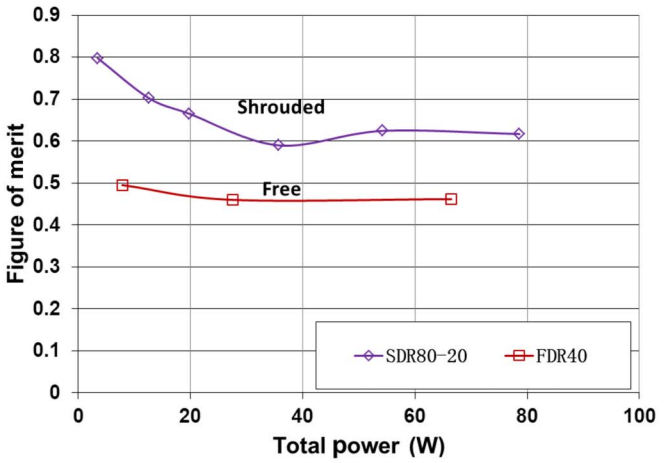


(d)

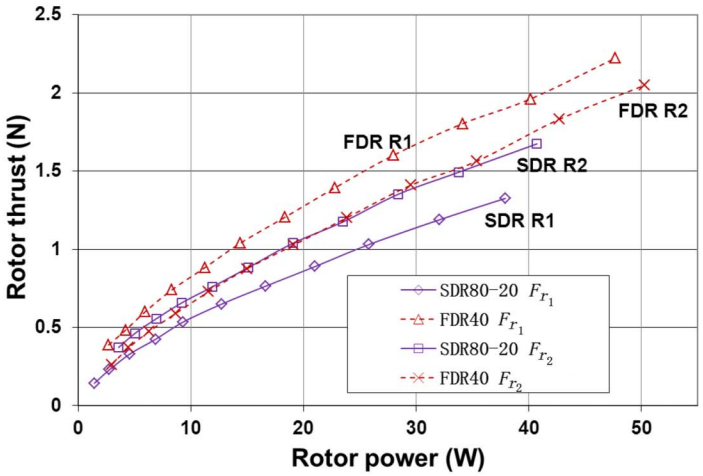


(e)

**Fig. 5. Different performance comparisons between shrouded and free systems: mass flow rate (a), total thrust (b), PL (c), FoM (d), and rotor thrust (e).**

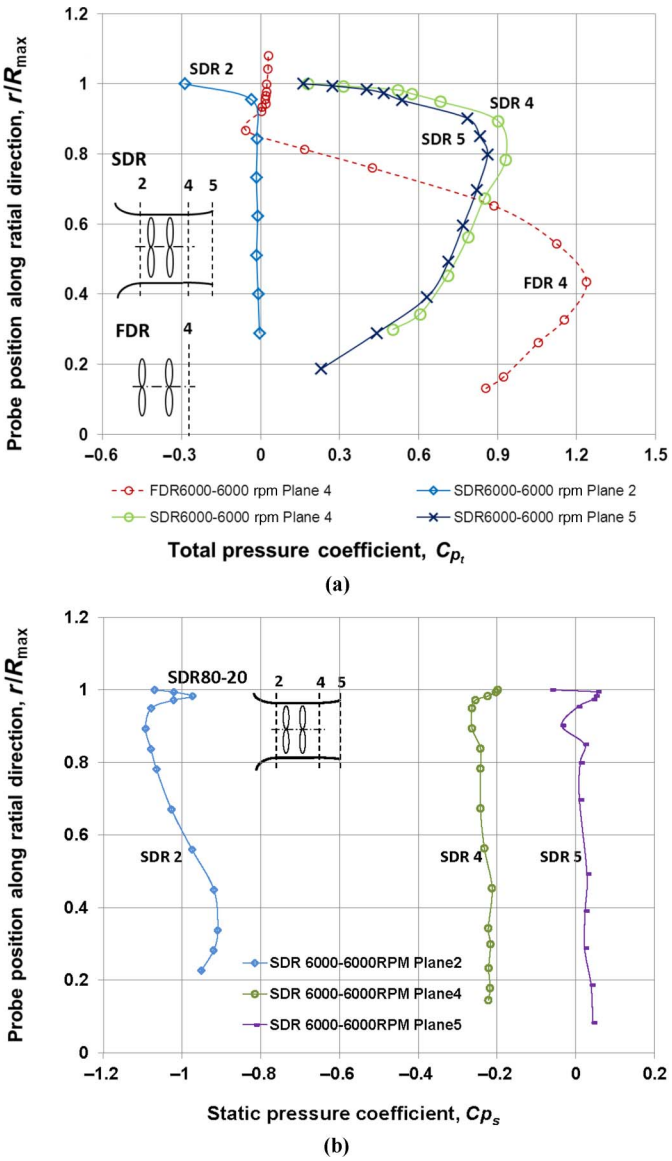


**Fig. 6. Total pressure, $C_{P_t}$ (a) and static pressure, $C_{P_s}$ (b) on different longitudinal planes, SDR80-20 and FDR40.**

upstream of the rotors. This lower static pressure greatly improves the ability of the system to aspirate mass flow.

Another interesting observation is the distribution of the pressure coefficient at the exit. The static pressure is nearly equal to zero, except the region near the center of the disk. This pressure distribution reflects the ability of the shroud to fully expand the flow at the outlet. The reduced wake velocity allows the shrouded system to make full use of the induced power. The uniform ambient pressure at the shroud exit is consistent with the assumptions present in the actuator disk theory.

*Shroud effects under different mass flow: Wall pressure tests.* The principal reason for the shroud's contribution to the total thrust is that the mass flow produces a favorable pressure distribution on the shroud surface (see Fig. 7). This figure provides two ways to present the static pressure coefficient measurement, $C_{p_s}$, on the shroud wall: Figure 7(a) plots the pressure distribution along the system axis, whereas Fig. 7(b) plots the pressure on the shroud profile for better visualization. In both representations, two rotors rotate at the same but opposite rotational speeds.

For the three different rotational speeds, generally, a low pressure is formed over the entire inner surface of the shroud, including a large depression peak at the shroud inlet. The flow is compressed all along the shroud with a pressure increase across two rotors. At the position close to the outlet, the pressure almost reaches to the atmospheric value. In hover, the flow cannot be purely axial in the inlet and due to the shroud profile curvature, the flow is accelerated. The first suction peak is hence formed just at the beginning of the shroud entrance, where an extremely low-pressure region occurs.

The effects of viscosity can be easily observed by comparing three rotor speeds (4000, 6000, and 8000 rpm). However, the first notable observation is the maximum mass flow (8000 rpm) producing the smallest $C_{P_s}$ upstream of the front rotor. Since the induced velocity was evaluated at the beginning of this work, and the same difference does not appear after the plane 2, it is concluded that the suction effect is weaker at higher speeds than at lower speeds due to the lower efficiency of the rotors, as the FoM data show in Fig. 7(a). Another possible reason for this trend in the inlet pressure is that a rotor operating at a high speed, such as 8000 rpm, may generate a blade resonance and the turbulence intensity surrounding the blade profile may become greater. The exact explanation of the deterioration of the wall pressure under high rotor speeds is not known, but should be explored further using computational fluid dynamics analysis which would avoid the physical limitations of the current setup.

In all three cases, a flow acceleration is observed at the end of the cylindrical section of the shroud, just before the beginning of the nozzle. More than a separation, a recirculation flow is constricting the cross-sectional area of the flow. The length of the cylindrical segment should be as short as possible to minimize the possibility of flow conditions conducive to producing restriction on the flow. Farther downstream, the pressure near the outlet approaches the ambient atmospheric pressure indicating the shroud nozzle design is well adapted to the flow streamlines resulting in a smooth recovery to the atmospheric pressure at the nozzle end.

Based on the shroud profile curvature and $C_{P_s}$ distribution in Fig. 7(b), the shroud inlet contributes most of the axial thrust integration for the shroud due to the suction peak. The cylindrical middle shroud section has no thrust contribution and should be as short as possible. The nozzle produces small negative thrust. However, the more important influence of the nozzle is on the mass flow rather than on the thrust.

*Effects of switching speeds: Wall and field pressure measurements.* Owing to the presence of the shroud and the rotor–rotor interaction, it has been noted that the performance of SDR systems is not strictly symmetric with respect to the line of $N_1 = N_2$ (see Fig. 4). This asymmetry implies that switching the two rotational speeds yields different performance. Only the configuration SDR80-40 has been tested in more detail to explore this effect, because its interrotor distance of 40 mm allows for measurements in between the rotors.

To emphasize the difference between the current system ($N_1 < N_2$) and the mirrored one (switched speeds: $N_1 > N_2$), the performance parameters such as thrust, power, torque, and PL should be presented for both systems. However, the common way to present performance versus the ratio $N_1/N_2$ results in "asymmetric" diagrams, which do not facilitate comparisons. The natural logarithm of the rotational velocity ratio $N_1/N_2$ is proposed to present different velocities rotor configurations. In Fig. 8, the plot becomes more "symmetric" by the linearization effect. It addresses the potential symmetry of the systems with switching speeds.

Comparing the measured variables where $N_1 < N_2$ to their reciprocal rotor speed condition $N_1 > N_2$, Figure 8 shows that the total thrust is generally symmetric. However, as it has been observed in the double-N diagram, the total thrust is improved under the condition $N_1 < N_2$ ($\ln(N_1/N_2) < 0$). For the largest disparity in switched speed (9000 and

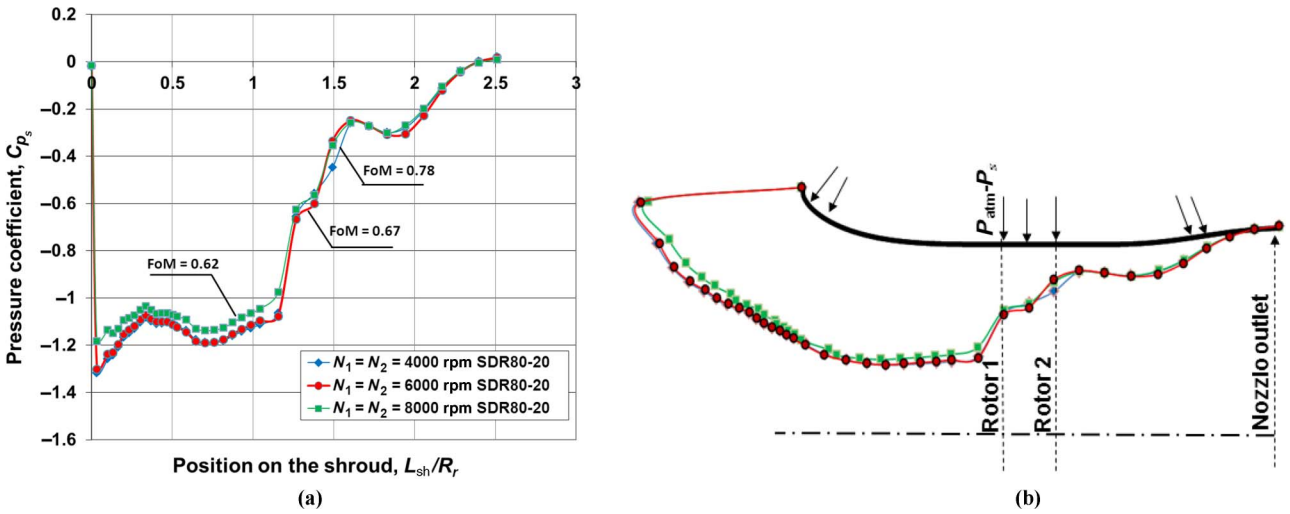


**Fig. 7. Wall pressure coefficients at varied speeds along shroud (a) and profile (b).**

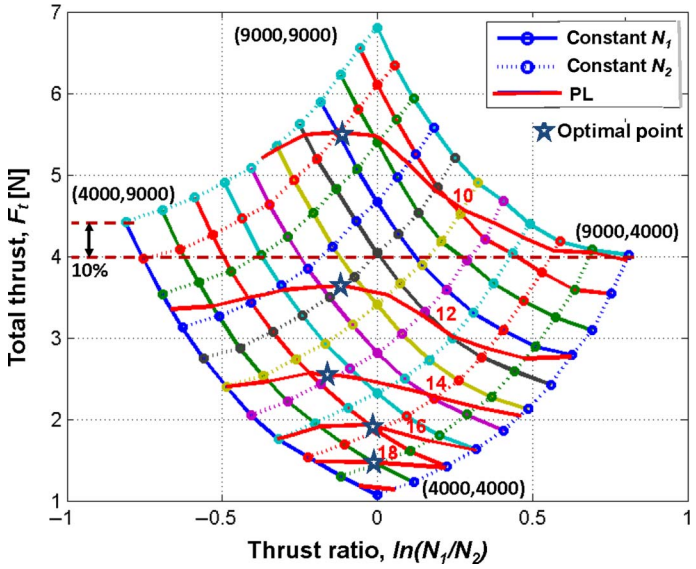


**Fig. 8. Total thrust versus $\ln(N_1/N_2)$, SDR80-40.**

4000 rpm), the thrust is increased by 10% for the configuration $N_1 < N_2$. In Fig. 8, the optimal thrust corresponds to the peak of the iso-PL lines and occurs at negative values of $\ln(N_1/N_2)$. In fact, owing to the asymmetric flow direction and the fundamental differences in the flow interactions of the two rotors, a perfect mirror behavior by exchanging rotor speeds should not be expected. Figure 8 indicates that the speed regime where the slower rotor is located upstream has a beneficial effect on PL.

To analyze the effect of the switching speeds, the flow characteristics were compared using two pairs of rotational speeds [$N_1 = 6000$ rpm, $N_2 = 9000$ rpm] and [$N_1 = 9000$ rpm, $N_2 = 6000$ rpm] identified as 6000–9000 and 9000–6000, respectively.

Figure 9(a) shows the comparison of the normalized total pressure distribution between these two speed combinations. Both speed combinations show losses due to blade tip vortices and the root swirl. The swirl effect near the root generates a greater total pressure drop, compared to tip vortices. The total pressure measured near the downstream rotor (plane 4) is disturbed by the obstruction of rotor support components. But the system where the upstream rotor operates at a faster speed suffers more total pressure loss.

Figure 9(b) presents the local shroud effects on the pressure coefficient for both rotor speed configurations. Switching the two rotors' speeds does not seem to introduce a gross difference on the inlet pressure distribution. However, the greater mass flow generated by the system with a slower upstream rotor produces a somewhat lower pressure just ahead of the upstream rotor. Even if the same pressure change $\Delta P$ is reached across two rotors (not for the same shaft power), this effect directly increases the shroud thrust.

Table 5 shows the averaged performance details for the two cases. Two main qualities, rotor FoM and PL for the whole system, are increased with the upstream rotor operating at slower speeds, even though the rotor power consumed is somewhat higher than the 9000–6000 case.

*Effects of rotor location IRD: Wall and field pressure measurements.* The comparison of overall performance between two rotor configurations with different IRDs, $0.2R_r$ and $0.4R_r$ (SDR80-20 and SDR80-40), is shown in Table 6. It reveals that the performance of SDR80-20 benefits a few grams per second in flow generation compared to SDR80-40. The rotors operate at a slightly higher efficiency.

As shown in Fig. 10(a), a slightly stronger depression situated upstream of the rotors is produced by a shorter interrotor distance. It allows SDR80-20 to generate slightly more mass flow. The pressure jumps ($\Delta C_{P1}$ and $\Delta C_{P2}$) produced by each rotor are different. $\Delta C_{P2}$ is generally greater than $\Delta C_{P1}$. The greater pressure jump generated by the second rotor explains why the zero total torque does not appear at $N_1 = N_2$, even though the thrust generated by each rotor is produced by static pressure. This observation also predicts the asymmetric performance of the two rotors although they operate at the same rotational speed. The greatest difference in static pressure occurs at the nozzle exit. The SDR80-20 configuration allows the nozzle to better adapt the flow. The static pressure of the downstream rotor wake is almost equal to the ambient pressure. However, shifting the downstream rotor farther aft creates a nonuniform flow field and seems to be more affected by the radial equilibrium.

Figure 10(b) presents the pressure coefficient measured on the shroud wall for both configurations. Compared to SDR80-40, the SDR80-20 configuration has a higher pressure coefficient at the inlet just ahead of the rotors (compare pressures at shroud position 0.6–1.2 in Fig. 10(b)), which implies less thrust generation by this region of the shroud. Likewise, a similar but less pronounced pressure difference between the two configurations is observed along the entire nozzle, implying that the nozzle of the SDR80-20 configuration produces less negative thrust

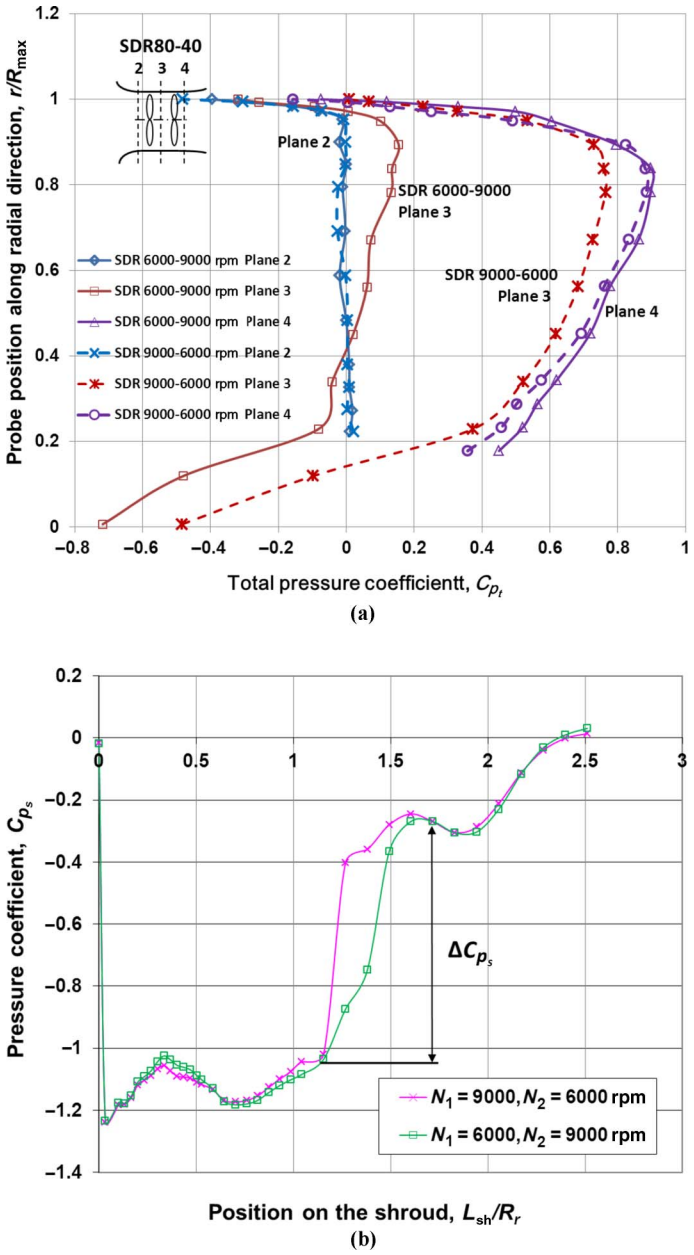


**Fig. 9. Comparison of total pressure, $C_{P_t}$, at different longitudinal planes (a) and static pressure, $C_{P_s}$, on shroud wall (b) between switched rotor speed pairs, SDR80-40.**

**Table 5. Performance comparison between systems with switched speeds, SDR80-40**

| | 6000–9000 | 9000–6000 |
|---|---|---|
| $W_{r_1}$ (W) | 9.23 | 39.62 |
| $W_{r_2}$ (W) | 42.44 | 9.17 |
| $F_{sh}$ (N) | 2.79 | 2.62 |
| PL (g/W) | 10.03 | 9.80 |
| $\dot{m}$ (kg/s) | 0.431 | 0.422 |
| FoM | 0.63 | 0.59 |

**Table 6. Performance comparison between systems with different rotor locations**

| SDR $D_{abs}$– IRD (mm) | 80-20 | 80-40 |
|---|---|---|
| $N_1, N_2$(rpm) | 6000, 6000 | 6000, 6000 |
| $F_{r_1}$ (N) | 0.535 | 0.550 |
| $F_{r_2}$ (N) | 0.760 | 0.752 |
| $W_{r_1}$ (W) | 9.32 | 9.63 |
| $W_{r_2}$ (W) | 11.89 | 12.23 |
| $F_{sh}$ (N) | 1.530 | 1.513 |
| PL (g/W) | 13.6 | 13.1 |
| $\dot{m}$ (kg/s) | 0.326 | 0.324 |
| FoM | 0.67 | 0.66 |

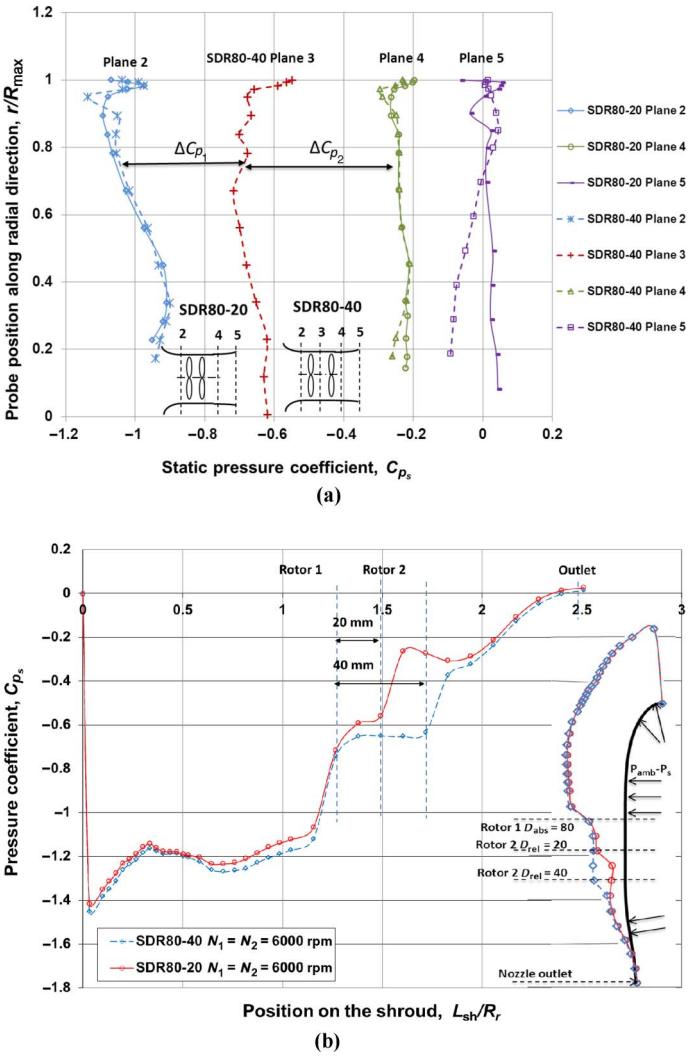


**Fig. 10. Comparisons of static pressure, $C_{P_s}$, at different longitudinal planes (a) and on shroud wall (b) between two rotor locations IRD = 20 and 40 mm.**

compared to the SDR80-40 configuration. Combined, the differences in the pressure acting on these two regions of the shroud may result in more thrust produced by the shroud for the SDR80-20 configuration compared to SDR80-40, because even though the difference in pressures measured at the region just ahead of the rotors is greater than at the nozzle, the projected area of the nozzle is much larger than the other region in question. However, we must acknowledge that the changes in

pressure just ahead of the rotors and at the nozzle may not fully account for the increase in shroud thrust and a complete explanation will require further study either experimentally or with computational fluid dynamics analysis. In an overall view, the effect of the interrotor distance on the global performance is negligible compared to other design parameters.

## Conclusions

An experimental exploration on both global performance and flow characteristics of a shrouded contrarotating rotor in hover was conducted on a newly designed test bed, able to measure separately the performance of three MAV elements: shroud, upstream rotor, and downstream contrarotating rotor. Based on the measured data, the main observations and key discussed results were made:

1) The comparison of the shrouded and the FDR systems at a given power reveals that the shroud presence substantially improves the whole system PL and rotor efficiency. The PL increase occurs due to the shroud's contribution to the total thrust as a result of a strong suction peak formed at the inlet. The capability to aspirate more mass flow for a given shaft power and fully expanding the flow in the nozzle allows shrouded systems to achieve higher rotor efficiency.

2) The most notable effect of the shroud's presence is that while the downstream rotor continues to produce the same amount of thrust, the upstream rotor thrust decreases, but the rotor system admits more mass flow, creating an additional thrust on the shroud, analogous to an efficient transfer of thrust from the upstream rotor to the shroud.

3) The shroud effectively creates a larger upstream stream tube area, reduces downstream stream tube contraction, while minimizing the total pressure loss from the blade tip vortices, which is a significant part of the loss as for FDR. The presence of the shroud results in a lower static pressure in front of the upstream rotor compared to the free rotor cases. This pressure change produces a suction peak on the shroud leading edge and allows the flow to reach ambient atmospheric pressure at the exit. All these fluid mechanisms contribute to the improvements given by the shroud.

4) Individual performance indicators for the SDR, such as rotor thrust, suggest that a general symmetry exists when the two rotational speeds are switched. However, this mirrored behavior is not perfect. The optimal performance is always found with the upstream rotor operating at a lower speed than the downstream rotor, thereby allowing the system to aspirate more mass flow and generate less pressure loss. Since the rotors generate a net torque when operating at the same speed, the final rotor configuration will have to consider not only the best PL but also the torque balance.

5) The effect of the interrotor distance is small for the current shroud design. As the downstream rotor shifts backwards, the nozzle cannot fully expand the flow. The static pressure at exit decreases and becomes nonuniform. All these phenomena indicate that a smaller interrotor distance improves system performance.

## Acknowledgments

The authors thank the China Scholarship Council and the Propulsion Laboratory of the Department of Aerodynamics, Energetics and Propulsion, Institut Supérieur de l'Aéronautique et de l'Espace for financial and facilities support.

## References

[1]Pines, D. J., and Bohorquez, F., "Challenges Facing Future Micro Air Vehicle Development," *Journal of Aircraft*, Vol. 43, (2), April 2006, pp. 290–305.

[2]Samuel, P., Sirohi, J., Rudd, L., Pines, D., and Perel, R., "Design and Analysis of a Micro Coaxial Rotorcraft," American Helicopter Society Vertical Lift Aircraft Design Conference, San Francisco, CA, January 19–21, 2000.

[3]Bohorquez, F., Samuel, P, Sirohi. J, Pines, D., and Rudd, L, "Design, Analysis and Hover Performance of a Rotary Wing Micro Air Vehicle," *Journal of the American Helicopter Society*, Vol. 48, (2), April 2003, pp. 80–90.

[4]Bohorquez, F., and Pines, D., "Rotor and Airfoil Design for Efficient Rotary Wing Micro Air Vehicles," American Helicopter Society 61st Annual Forum Proceedings, Grapevine, TX, June 1–3, 2005.

[5]Coleman, C. P., "A Survey of Theoretical and Experimental Coaxial Rotor Aerodynamic Research," NASA TN 3675, 1997.

[6]Hein, B. R., and Chopra, I., "Hover Performance of a Micro Air Vehicle: Rotors at Low Reynolds Number," *Journal of the American Helicopter Society*, Vol. 52, (3), July 2007, pp. 254–262.

[7]Tsuzuki, N., Sato, S., and Abe, T., "Design Guidelines of Rotary Wings in Hover for Insect-Scale Micro Air Vehicle Applications," *Journal of Aircraft*, Vol. 44, (1), January 2007, pp. 252–263.

[8]Grasmeyer, J. M., and Keennon, M. T., "Development of the Black Widow Micro Air Vehicle," AIAA 2001-0127, 39th Aerospace Science Meeting Exhibit, Reno, NV, January 8–11, 2001.

[9]Martin, P. B., and Boxwell, D. A., "Design, Analysis, and Experiments on a 10-Inch Ducted Rotor VTOL UAV," AHS International Specialist's Meeting on Unmanned Rotorcraft, Phoenix, AZ, January 18–20, 2005.

[10]Zhao, H. W., and Bil, C., "Aerodynamic Design and Analysis of a VTOL Ducted-Fan UAV," 26th AIAA Applied Aerodynamics Conference, Honolulu, HI, August 18–21, 2008.

[11]Toshiyuki. S., and Abraham, E., "Design and Performance Analysis of Ducted Fans for Micro UAV Applications," AHS International Specialists' Meeting on Unmanned Rotorcraft: Design, Control, and Testing, Phoenix, AZ, January 2005.

[12]Kruger, W., "On Wind Tunnel Tests and Computations Concerning the Problem of Shrouded Propellers," NACA TM 1202, 1949.

[13]Vuillet, A., and Morelli, F., "New Aerodynamic Design of the Fenestron for Improved performance," 12th European Rotorcraft Forum, Garmisch-Partenkirchen, Germany, September 22–25, 1986.

[14]Black, D. M., and Wainauski, H. S., "Shrouded Propellers—A Comprehensive Performance Study," AIAA 5th Annual Meeting and Technical Display, Philadelphia, PA, October 21–24, 1968.

[15]Rajneesh, S., and Surya, D., "Shape Optimization of a Ducted Rotor System for Aerodynamic Performance," 49th AIAA Aerospace Sciences Meeting including the New Horizons Forum and Aerospace Exposition, Orlando, FL, January 4–7, 2011.

[16]Pereira, J., and Chopra, I., "Performance and Surface Pressure Measurements on A MAV-Scale Shrouded Rotor in Translational Flight," Proceedings American Helicopter Society 63rd Annual Forum Proceedings, Virginia Beach, VA, May 1–3, 2007.

[17]Pereira, J., and Chopra, I., "Effect of Shroud Design Variables on Hover Performance of a Shrouded Rotor for Micro Air Vehicle Applications," AHS International Specialists' Meeting on Unmanned Rotorcraft, Chandler, AZ, January 18–20, 2005.

[18]Hrishikeshavan, V., Sirohi, J., Tishchenko, M., and Chopra, I., "Design, Development, and Testing of a Shrouded Single-Rotor Micro Air Vehicle with Antitorque Vanes," *Journal of the American Helicopter Society,* **56**, 012008 (2011).

[19]Lakshminarayan, V. K., and Baeder, J. D., "Computational Investigation of Microscale Shrouded Rotor Aerodynamics in Hover," *Journal of the American Helicopter Society*, **56**, 042002 (2011).

[20]Lee, T. E., Leishman, J. G., and Rand, O., "Design and Testing of a Ducted Coaxial Rotor System for Application to a Micro Aerial Vehicle," American Helicopter Society International 66th Annual Forum Proceedings, Phoenix, AZ, May 10–13, 2010.

[21]Huo, C., Barénes, R., and Gressier, J., "Effect Study of Design Variables on Hover Performance of Long Shrouded Contra-rotating Rotors," 46th Symposium of Applied Aerodynamics Aerodynamics of Rotating Bodies, Orleans, France, March 28–30, 2011.

[22]Huo, C., Barénes, R., Gressier, J., and Grondon, G., "Numerical Study on Parametrical Design of Long Shrouded Contra-rotating Propulsion System in Hovering," International Conference on Mechanical and Aerospace Engineering, Venice, Italy, November 28–30, 2011.

[23]Drela, M., and Youngren, H., "Axisymmetric Analysis and Design of Ducted Rotors," Report, Ducted Coaxial Rotor Design, ISAE Institut Supérieur de l'Aéronautique et de l'Espace, December 2005.

[24]Betz. A., "Airscrews with Minimum Energy Loss," Report, Kaiser Wilhelm Institute for Flow Research, 1919.

[25]Glauert. H., *Elements of Airfoil and Airscrew Theory*, Cambridge University Press, Cambridge, UK, 1937.

[26]Leishman, J. G., and Ananthan, S., "An Optimum Coaxial Rotor System for Axial Flight," *Journal of the American Helicopter Society*, Vol. 53, (4), October 2008, pp. 366–381.

[27]Kline, S. J., and McClintock, F. A., "Describing Uncertainties in Single-Sample Experiments," *Mechanical Engineering*, Vol. 75, (1), January 1953, pp. 3–8.

[28]Huo C., "Experimental and Numerical Analysis of a Shrouded Contrarotating Coaxial Rotor in Hover," Ph.D. thesis, Institut Supérieur de l'Aéronautique et de l'Espace, PRES, Toulouse, France, March 26, 2012.

[29]Bohorquez, F., and Pines, D., "Rotor and Airfoil Design for Efficient Rotary Wing Micro Air Vehicles," American Helicopter Society 61st Annual Forum Proceedings, Grapevine, TX, June 1–3, 2005.